

©Copyright 2023

Anthony Su

# Modeling of Active Aeroservoelastic Systems

Anthony Su

A thesis

submitted in partial fulfillment of the  
requirements for the degree of

Master of Science in Aeronautics & Astronautics

University of Washington

2023

Committee:

Name of Chairperson

First committee member

Next committee member

etc

Program Authorized to Offer Degree:

William E. Boeing Department of Aeronautics & Astronautics

University of Washington

**Abstract**

Modeling of Active Aeroservoelastic Systems

Anthony Su

Chair of the Supervisory Committee:

Title of Chair Name of Chairperson

William E. Boeing Department of Aeronautics & Astronautics

Lorem ipsum dolor sit amet, consectetur adipiscing elit. Nunc et maximus tortor, eget congue lectus. Suspendisse quis sodales mi. In faucibus libero vel condimentum ornare. Suspendisse a erat porta justo suscipit porttitor at et magna. Duis vitae egestas eros. Curabitur enim ex, tempus et nunc eget, interdum convallis nisi. In hac habitasse platea dictumst. Curabitur a nisl non turpis fermentum tincidunt. Vestibulum ante ipsum primis in faucibus orci luctus et ultrices posuere cubilia curae; Curabitur euismod molestie nulla, non molestie sem hendrerit vel. Pellentesque dapibus vulputate urna et dignissim. Morbi condimentum, velit quis fermentum faucibus, velit tellus scelerisque enim, a feugiat quam nulla in enim. Duis sed neque eget lorem condimentum varius vitae quis magna. Cras viverra posuere lorem, in fermentum leo porta a. Nam accumsan neque ut pretium volutpat.

# TABLE OF CONTENTS

	Page
List of Figures . . . . .	iii
List of Tables . . . . .	iv
Nomenclature . . . . .	v
Chapter 1: Introduction . . . . .	1
Chapter 2: System Description . . . . .	2
Chapter 3: Dynamic System Modeling . . . . .	6
3.1 Equations of Motion . . . . .	6
3.2 The Roger Approximation . . . . .	7
3.3 Output Modeling . . . . .	8
3.4 Actuation and Sensing Dynamics . . . . .	8
Chapter 4: Finite Element Modeling . . . . .	12
Chapter 5: Ground Vibration Testing . . . . .	13
5.1 Test Setup . . . . .	13
5.1.1 Sensor Placement . . . . .	14
5.2 Generating Frequency Response Functions . . . . .	15
5.2.1 Time-Domain Post-Processing . . . . .	15
5.2.2 Computing Frequency Response Functions . . . . .	15
5.3 Determining Modal Properties . . . . .	16
5.3.1 Computing Natural Frequencies . . . . .	16
5.3.2 Computing Damping Ratios . . . . .	17

Chapter 6:	Wind Tunnel Validation and Model Tuning . . . . .	19
Chapter 7:	Results . . . . .	20
Chapter 8:	Conclusion . . . . .	21
Appendix A:	Frequency Response Functions . . . . .	22

## LIST OF FIGURES

Figure Number	Page
2.1 MARGE structural configuration . . . . .	3
2.2 MARGE sensing and actuation configuration . . . . .	4
2.3 Univeristy of Washington 3x3 low-speed wind tunnel . . . . .	5
3.1 Integrated model of actuation, plant, and sensing in a control loop . . . . .	9
3.2 Padé approximant of the pure-delay response of the wind tunnel gust vanes .	10
5.1 Accelerometer placement in ground vibration testing of MARGE . . . . .	14

## LIST OF TABLES

Table Number	Page
4.1 Area moment of inertia of beam finite elements . . . . .	12
5.1 Experimental Natural Modes . . . . .	18

# NOMENCLATURE

## Abbreviations

CZT	=	chirp Z-transform
DFT	=	discrete Fourier transform
FEA	=	finite element analysis
FRF	=	frequency response function
GLA	=	gust load alleviation
GVT	=	ground vibration testing
HIL	=	hardware-in-the-loop
LE	=	leading edge
MARGE	=	Model for Aeroelastic Response to Gust Excitation
SISO	=	single-input single-output
TE	=	trailing edge

## Variables

$b$	=	reference semi-chord
$j$	=	imaginary unit
$k$	=	reduced frequency
$s$	=	Laplace variable

## Subscripts

$s$	=	structural (flexible) component
$c$	=	control (rigid) component
$p$	=	plant
act	=	actuator



$\text{sens}$  = sensor

### **Notation**

$[ \quad ]$  = matrix

$\{ \quad \}$  = column vector

## ACKNOWLEDGMENTS

Lorem ipsum dolor sit amet, consectetur adipiscing elit. Sed sed erat vehicula elit sollicitudin ultrices at nec ligula. Sed non massa eget nibh pellentesque dapibus non at ante. Integer augue lacus, tincidunt vel sollicitudin fringilla, accumsan vitae lorem. Nunc eleifend scelerisque consectetur. Etiam justo nibh, hendrerit nec mattis non, tincidunt lacinia augue. Morbi ac enim hendrerit, iaculis ante eget, tincidunt massa. Morbi at justo sapien. Donec pulvinar urna id orci sodales, in ornare dolor venenatis. Quisque rutrum mi ac ornare tincidunt.

## DEDICATION

to Lorem Ipsum, my dear friend

## Chapter 1

# INTRODUCTION

talk about aeronautics

talk about aerodynamics

talk about structural dynamics

talk about aeroelasticity

talk about control

talk about aeroservoelasticity

talk about MARGE

The goal of this project was to obtain a state-space model of MARGE in order to demonstrate low-cost active aeroservoelastic control.

The remainder of this document is organized as follows: Lorem Ipsum.

## Chapter 2

### SYSTEM DESCRIPTION

The subject of this study's modeling effort is the Model for Aeroelastic Response to Gust Excitation (MARGE). MARGE is a flexible half-span wing-body-tail wind tunnel model which is capable of rigid-body rotation in the pitch axis. It was designed to allow rapid and accessible testing of gust alleviation control laws. Thus, it is of a simple and affordable construction. Details of the original design and construction of MARGE can be found in [?].

The structure of MARGE consists of flexible beams encapsulated by lightweight aerodynamic shells. The wing and tail spars are made of aluminum while the fuselage is made of steel. The aerodynamic shells are made of polylactic acid (PLA) and form a symmetrical NACA 0012 airfoil. There is a brass mass fixed at the wing tip to bring the structure's natural frequencies to the designed magnitude. The wing is joined to the fuselage at its root and the entire assembly rotates about a shaft which is suspended from the hanging sub-assembly with bearings. A diagram of the structural configuration of MARGE is shown in Fig. 2.1.

MARGE has three actuators: two servo-actuated control surfaces on the wing and one servo-actuated elevator on the tail. There are also two gust vanes installed upstream of the test section in the 3x3 low-speed wind tunnel. The gust vanes are capable of moving in unison to generate discrete or continuous gusts.

MARGE has five sensors. There are two unidirectional accelerometers at the wingtip, one ahead of the wing spar and one aft of the wing spar. There is another unidirectional accelerometer at the tip of the tail. There is a strain gauge at the wing root. Finally, there is a hall effect sensor inside the hanging sub-assembly by the model's rotating shaft. There is a magnet fixed to the shaft which allows the hall effect sensor to measure the rotation of the shaft. A diagram of the sensing and actuation configuration of MARGE is shown in Fig.

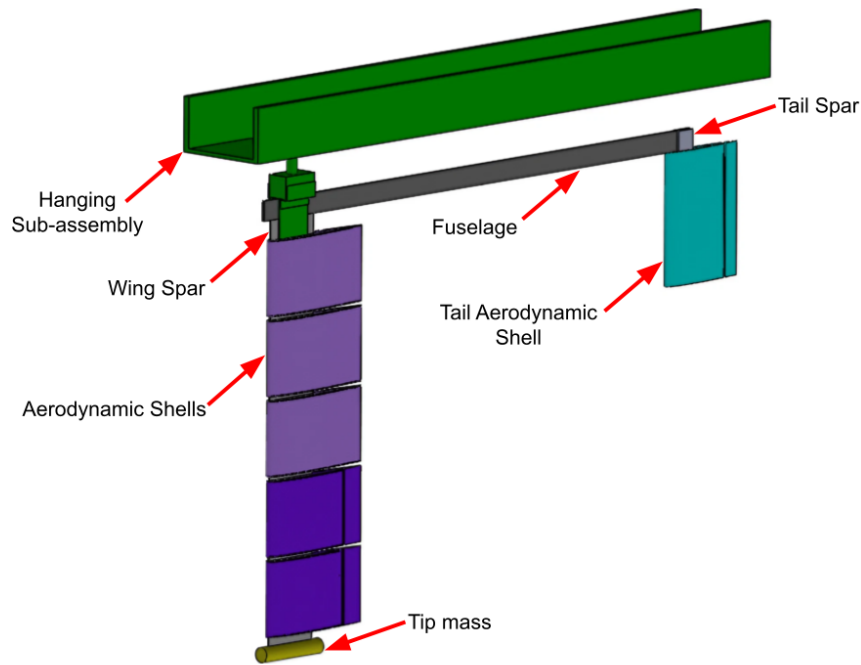


Figure 2.1: MARGE structural configuration

## 2.2.

Note that the sensor configuration is modified from the original design specified in [?]. The original design featured potentiometers on the control surfaces and a strain gauge on the fuselage. It also lacked the accelerometer on the tail. The potentiometers and the fuselage strain gauge were previously removed because they were found to be unnecessary. The accelerometer on the tail was previously added with the intent of capturing fuselage and tail flexible motions.

MARGE is designed to fit into the University of Washington's 3x3 low-speed wind tunnel. The 3x3 low-speed wind tunnel is an open-loop wind tunnel capable of speeds up to 60 m/s. The wind tunnel has flow straighteners, a 9:1 contraction, gust vanes, and a 3 ft. by 3 ft. by 8 ft. test section. Further details about the 3x3 low-speed wind tunnel can be found in [?]. When installed, MARGE hangs vertically from the ceiling of the test section. A diagram

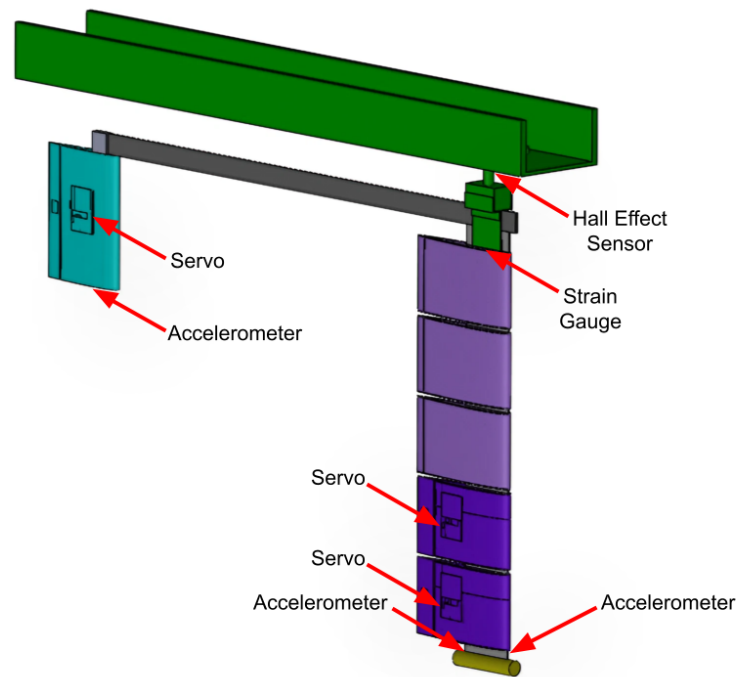


Figure 2.2: MARGE sensing and actuation configuration

indicating the locations of key features of the 3x3 low-speed wind tunnel is shown in Fig. 2.3.

The physical interface to MARGE's acutation and sensing is a National Instruments <insert DAQ> coupled with a National Instruments BNC-2110 terminal block. The exceptions to this are the gust vanes, which are controlled through the HTTP protocol on the local network. Data is sent to and from these interfaces through Simulink Real-Time.

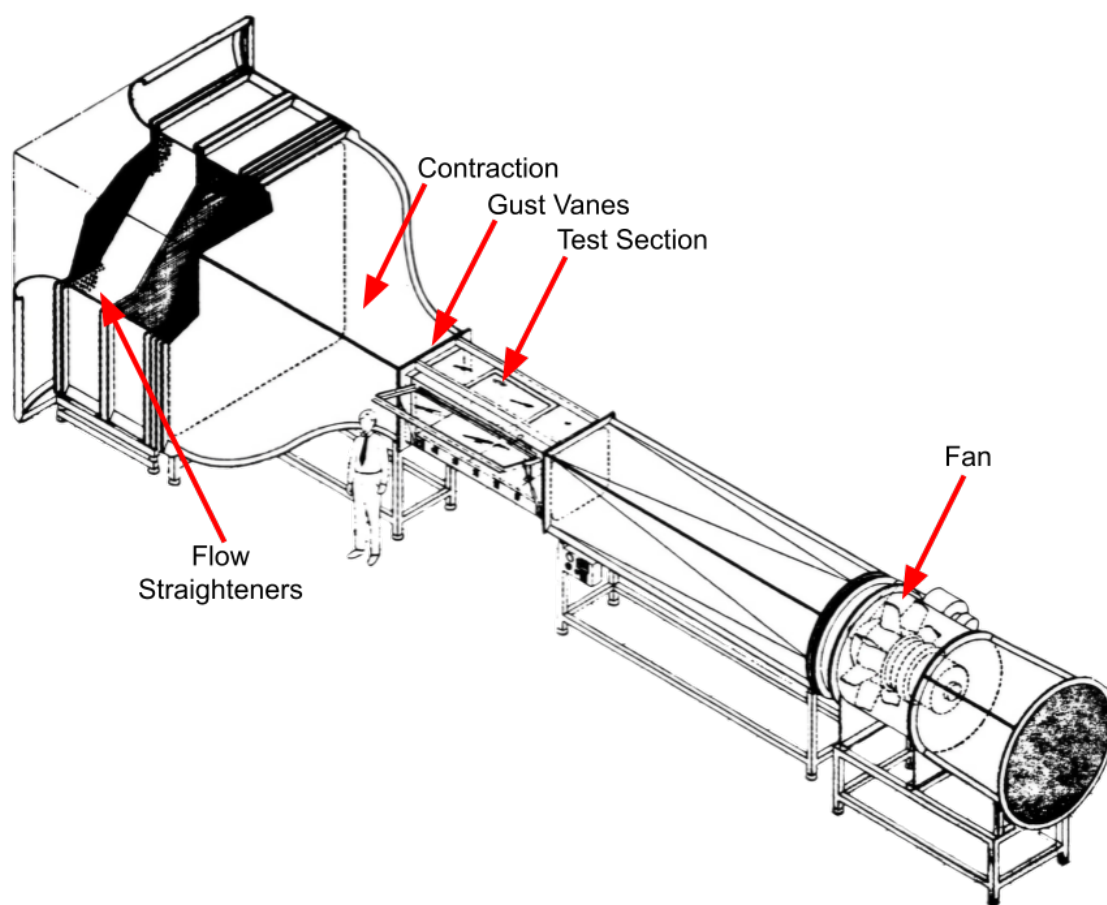


Figure 2.3: University of Washington 3x3 low-speed wind tunnel



## Chapter 3

### DYNAMIC SYSTEM MODELING

The goal of this section is to obtain a preliminary state-space model for the aeroservoelastic system in the form

$$\{\dot{x}\} = [A]\{x\} + [B]\{u\} \quad (3.1)$$

$$\{y\} = [C]\{x\} + [D]\{u\} \quad (3.2)$$

based on first principles.

#### 3.1 *Equations of Motion*

The equations of motion for the general structural dynamic system with damping and forcing in the Laplace domain are

$$s^2[M]\{q(s)\} + s[C]\{q(s)\} + [K]\{q(s)\} = \{f(s)\} \quad (3.3)$$

where  $\{q\}$  is the state expressed in the generalized modal coordinates,  $\{f(s)\}$  is the generalized external forcing, and  $[M]$ ,  $[C]$ , and  $[K]$  are generalized mass, damping, and stiffness matrices respectively. Note that the modal coordinates include both elastic motions (of the structure) and rigid-body motions (of the structure and the control surfaces).

The forcing for the aeroservoelastic wing can be decomposed into the aerodynamic forcing due to the state and the forcing from actuator hinge moments:

$$s^2[M]\{q(s)\} + s[C]\{q(s)\} + [K]\{q(s)\} = q_D[A(s)]\{q(s)\} + \begin{Bmatrix} \{0\} \\ \{H_c\} \end{Bmatrix} \quad (3.4)$$

where  $[A(s)]$  is the aerodynamic influence matrix for the state and  $H_c$  is the hinge moment's influence.

The whole system can be further decomposed into structural and control modes:

$$\begin{aligned} & \left( s^2 \begin{bmatrix} [M_{ss}] & [M_{sc}] \\ [M_{cs}] & [M_{cc}] \end{bmatrix} + s \begin{bmatrix} [C_{ss}] & [C_{sc}] \\ [C_{cs}] & [C_{cc}] \end{bmatrix} + \begin{bmatrix} [K_{ss}] & [K_{sc}] \\ [K_{cs}] & [K_{cc}] \end{bmatrix} \right) \begin{Bmatrix} \{q_s(s)\} \\ \{q_c(s)\} \end{Bmatrix} \\ &= q_D \begin{bmatrix} [A_{ss}(s)] & [A_{sc}(s)] \\ [A_{cs}(s)] & [A_{cc}(s)] \end{bmatrix} \begin{Bmatrix} \{q_s(s)\} \\ \{q_c(s)\} \end{Bmatrix} + \begin{Bmatrix} \{0\} \\ \{H_c\} \end{Bmatrix} \quad (3.5) \end{aligned}$$

The control modes are those corresponding to rigid-body motions of control surfaces. The structural modes are all other modes, including flexible-body modes and rigid-body modes of the entire model.

It is assumed that the dynamics of the control modes are completely determined by the control inputs and the inputs are not directly affected by the control modes, i.e. the actuators are irreversible controls. Then, interest is only in the dynamics of the structural modes:

$$\begin{aligned} & \left( s^2 \begin{bmatrix} [M_{ss}] & [M_{sc}] \end{bmatrix} + s \begin{bmatrix} [C_{ss}] & [C_{sc}] \end{bmatrix} + \begin{bmatrix} [K_{ss}] & [K_{sc}] \end{bmatrix} \right) \begin{Bmatrix} \{q_s(s)\} \\ \{q_c(s)\} \end{Bmatrix} \\ &= q_D \begin{bmatrix} [A_{ss}(s)] & [A_{sc}(s)] \end{bmatrix} \begin{Bmatrix} \{q_s(s)\} \\ \{q_c(s)\} \end{Bmatrix} \quad (3.6) \end{aligned}$$

Note that since the control modes are rigid-body modes, they have no stiffness ( $[K_{cc}]$ ,  $[K_{sc}]$ , and  $[K_{cs}]$  are zero) and the equations of motion further simplify to

$$\begin{aligned} & \left( s^2 \begin{bmatrix} [M_{ss}] & [M_{sc}] \end{bmatrix} + s \begin{bmatrix} [C_{ss}] & [C_{sc}] \end{bmatrix} + \begin{bmatrix} [K_{ss}] & [0] \end{bmatrix} \right) \begin{Bmatrix} \{q_s(s)\} \\ \{q_c(s)\} \end{Bmatrix} \\ &= q_D \begin{bmatrix} [A_{ss}(s)] & [A_{sc}(s)] \end{bmatrix} \begin{Bmatrix} \{q_s(s)\} \\ \{q_c(s)\} \end{Bmatrix} \quad (3.7) \end{aligned}$$

### 3.2 The Roger Approximation

The aerodynamic influence matrix  $[A]$  is a nonlinear function of reduced frequency  $k$ . In order to obtain a linear state-space system, it must be approximated as an analytic function of  $k$ .

The Roger approximation [?] is a method of generating a rational function approximation of the aerodynamic influence matrix in the form

$$[A(jk)] \approx [\bar{P}_0] + jk[\bar{P}_1] + (jk)^2[\bar{P}_2] + \sum_{n=1}^{N_{\text{lag}}} \frac{jk}{jk + \bar{\beta}_n} [\bar{P}_{n+2}] \quad (3.8)$$

where  $[P]$  are the unknown real-valued matrices that are fit to the tabulated matrices. Aside from the zeroth, first, and second order terms, there are  $N_{\text{lag}}$  additional "lag term" approximating functions which are defined by their respective constants  $\bar{\beta}$ . The constants  $\bar{\beta}$  are pre-determined

Given a tabulated set of known aerodynamic influence matrices across a range of reduced frequencies  $k$ ,

For the  $(1, 1)$  element of an aerodynamic influence matrix  $[A]$

### 3.3 Output Modeling

### 3.4 Actuation and Sensing Dynamics

When developing a model that is used for control design, the dynamics of the actuators and sensors must be accounted for. The output of the control law will be fed not into the plant, but the imperfect actuators. The input of the control law will come not directly from the plant, but from the imperfect sensors. The imperfect actuators and sensors can be accounted for in modeling by combining the actuator, plant, and sensor models into an integrated system model that can then be used for control design; see Fig. 3.4 for a block diagram of this system of systems.

The servo-actuated control surfaces on the wing and tail are known (from [?]) to have dynamics according to the following transfer function<sup>1</sup>:

$$G(s) = \frac{1461}{s^2 + 62.2s + 1461} \quad (3.9)$$

---

<sup>1</sup>The numerator of this transfer function differs from that defined in [?] because the actuator is calibrated to have unity DC gain before use.

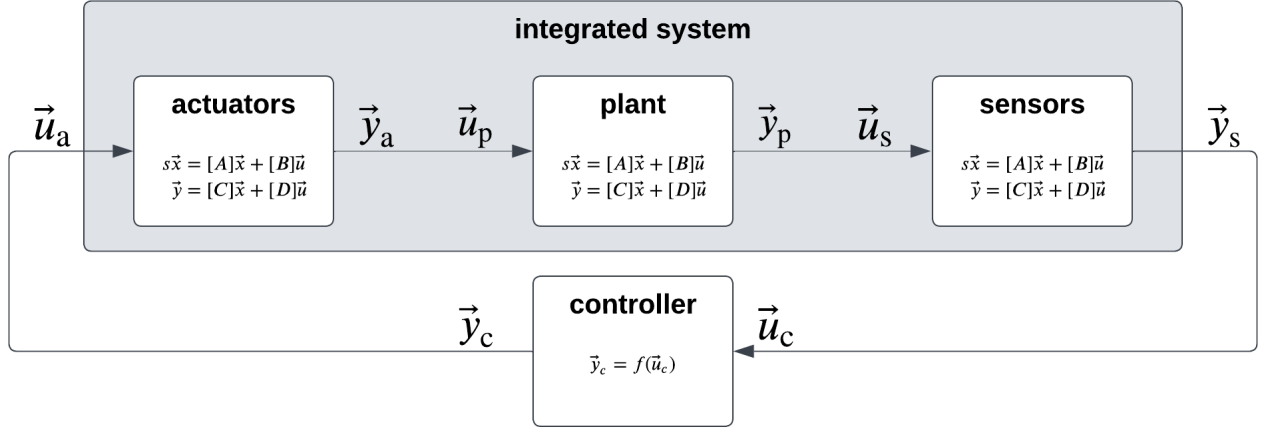


Figure 3.1: Integrated model of actuation, plant, and sensing in a control loop

This transfer function was then converted to the following equivalent state-space representation:

$$\begin{aligned} s\{x\} &= \begin{bmatrix} -62.2 & -1461 \\ 1 & 0 \end{bmatrix} \{x\} + \begin{bmatrix} 0 \\ 1 \end{bmatrix} u \\ y &= \begin{bmatrix} 0 & 1461 \end{bmatrix} \{x\} \end{aligned} \quad (3.10)$$

where  $u$  is the input,  $y$  is the output, and  $\{x\}$  is the internal state of the actuator.

The wind tunnel gust vanes were measured to have no internal dynamics except for a pure time delay of 0.34 seconds. This pure delay was approximated as a second-order transfer function using a Padé approximant:

$$G(s) = \frac{s^2 - 176.47s + 10381}{s^2 + 176.47s + 10381} \quad (3.11)$$

The Padé approximant matches the pure delay's response well in the frequency range of interest ( $<20$  Hz); the step response and phase shift behavior of a pure delay and the Padé approximant are compared in Fig. 3.4.

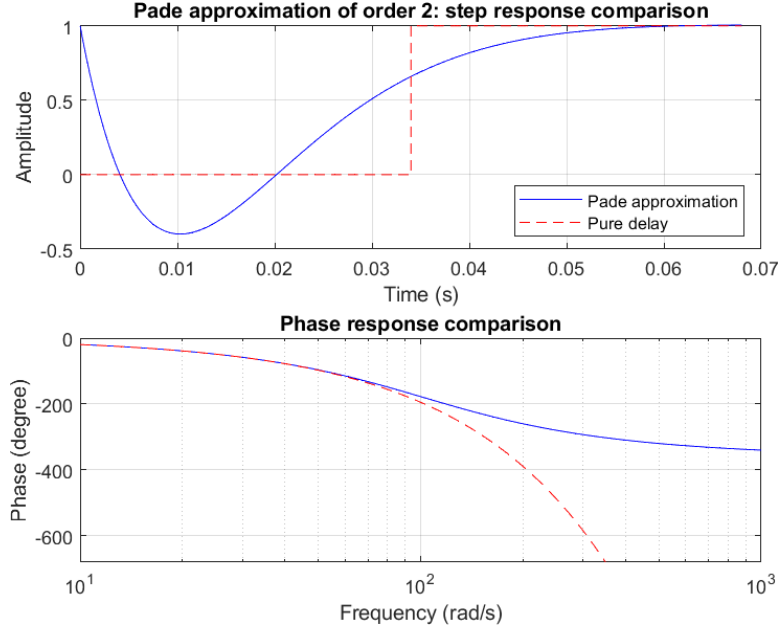


Figure 3.2: Padé approximant of the pure-delay response of the wind tunnel gust vanes

This transfer function was then converted to the following equivalent state-space representation:

$$\begin{aligned} s\{x\} &= \begin{bmatrix} -176.47 & -10381 \\ 1 & 0 \end{bmatrix} \{x\} + \begin{bmatrix} 1 \\ 0 \end{bmatrix} u \\ y &= \begin{bmatrix} -352.94 & 0 \end{bmatrix} \{x\} + \begin{bmatrix} 1 \end{bmatrix} u \end{aligned} \quad (3.12)$$

where  $u$  is the input,  $y$  is the output, and  $\{x\}$  is the internal state of the actuator.

The state-space models for the four actuators (three servo-actuated control surfaces and one pair of wind tunnel gust vanes) are combined to form one combined state-space model for all actuators with input, output, and state

$$\{u_{\text{act}}\} = \begin{bmatrix} u_1 \\ u_2 \\ u_3 \\ u_4 \end{bmatrix} \quad \{y_{\text{act}}\} = \begin{bmatrix} y_1 \\ y_2 \\ y_3 \\ y_4 \end{bmatrix} \quad \{x_{\text{act}}\} = \begin{bmatrix} \{x\}_1 \\ \{x\}_2 \\ \{x\}_3 \\ \{x\}_4 \end{bmatrix} \quad (3.13)$$

respectively. The combined actuation state-space model is then

$$\begin{aligned}
 \{x_{\text{act}}\} &= \begin{bmatrix} [A_1] & & & \\ & [A_2] & & \\ & & [A_3] & \\ & & & [A_4] \end{bmatrix} \{x_{\text{act}}\} + \begin{bmatrix} [B_1] & & & \\ & [B_2] & & \\ & & [B_3] & \\ & & & [B_4] \end{bmatrix} \{u_{\text{act}}\} \\
 \{y_{\text{act}}\} &= \begin{bmatrix} [C_1] & & & \\ & [C_2] & & \\ & & [C_3] & \\ & & & [C_4] \end{bmatrix} \{x_{\text{act}}\} + \begin{bmatrix} [D_1] & & & \\ & [D_2] & & \\ & & [D_3] & \\ & & & [D_4] \end{bmatrix} \{u_{\text{act}}\}
 \end{aligned} \tag{3.14}$$

where the  $[A]$ ,  $[B]$ ,  $[C]$ , and  $[D]$  system matrices for the two types of actuators are defined above in Eq. 3.10 and 3.12. This then forms the actuator block shown in Fig. 3.4.

A similar process would be appropriate for a set of imperfect sensors. However, the high-rate sensors used in MARGE have approximately no dynamics in the frequency range of interest. Thus, the sensor response was approximated as

$$\{y_{\text{sens}}\} = \{u_{\text{sens}}\} \tag{3.15}$$

In other words, the output of the sensor was taken as the output of the plant. This then forms the sensor block shown in Fig. 3.4.

## Chapter 4

**FINITE ELEMENT MODELING**

An aeroelastic finite element model of MARGE was previously constructed using NAS-TRAN. The model captures MARGE, the wind tunnel test section walls, and the gust vanes.

The wing structure and tail structure were each modeled as a single chain of Euler-Bernoulli beam elements along their respective spar.

The area moments of inertia of the beam elements in the finite element model are reported in Table 4.1.

Table 4.1: Area moment of inertia of beam finite elements

	$I_1, \text{ m}^4$	$I_2, \text{ m}^4$	$J, \text{ m}^4$
wing spar	$2.541 \times 10^{-11}$	$5.853 \times 10^{-8}$	$5.856 \times 10^{-8}$
tail spar	$1.829 \times 10^{-9}$	$1.301 \times 10^{-8}$	$1.484 \times 10^{-8}$
fuselage	$7.452 \times 10^{-11}$	$4.476 \times 10^{-9}$	$4.550 \times 10^{-9}$
rigid	$2.541 \times 10^{-11}$	$5.853 \times 10^{-8}$	$5.856 \times 10^{-8}$

The aerodynamic loads on the NASTRAN model are based on the doublet-lattice model (DLM) of aerodynamics. This linear aerodynamic model assumes incompressible, inviscid, irrotational flow around thin lifting surfaces. The loads were transferred from the aerodynamic panels to the structural elements with NASTRAN

The loads on the finite element model were determined using doublet-lattice lifting surface theory which is <insert>

The loads on the aerodynamic panels were transferred to the structural nodes via a spline interpolation.

## Chapter 5

### GROUND VIBRATION TESTING

Ground vibration testing (GVT) was performed to validate the preliminary finite-element model of MARGE. The frequency responses of accelerometers to an impulse input were generated from the experimental data. Using these, the natural frequencies and the damping ratios of dynamic modes of the system were determined.

Two sets of data were collected. The first set of data was collected with MARGE as designed, including the rigid-body pitching mode. This data was used to determine the damping ratios of the modes. The second set of data was collected with the root of the MARGE wing clamped to eliminate the rotational rigid-body mode. This was done to enable data acquisition of flexible-body modes without exciting and losing energy to the rigid-body mode. This data was used to tune the finite-element model and to determine the damping ratios of the wing bending modes.

#### **5.1 Test Setup**

The equipment used for the test include:

- PCB Piezotronics ICP Impact Hammer Model 086C03
- PCB Piezotronics ICP Accelerometer Model 352C22
- National Instruments Breakout <insert>
- National Instruments DAQ Module <insert>



The impact hammer and accelerometers were connected to the DAQ system which was connected to a personal computer. The computer recorded data from the DAQ system using the Data Acquisition Toolbox for MATLAB.

### 5.1.1 Sensor Placement

The accelerometers were placed in locations such that all of the flexible natural modes of interest were observable. This was done by placing accelerometers near anti-nodal points of the natural modes as predicted by the preliminary finite-element model. The accelerometer locations for the two sets of testing are shown in Fig. 5.1. The impact hammer hits were also placed at these same locations on the structure as the accelerometers.

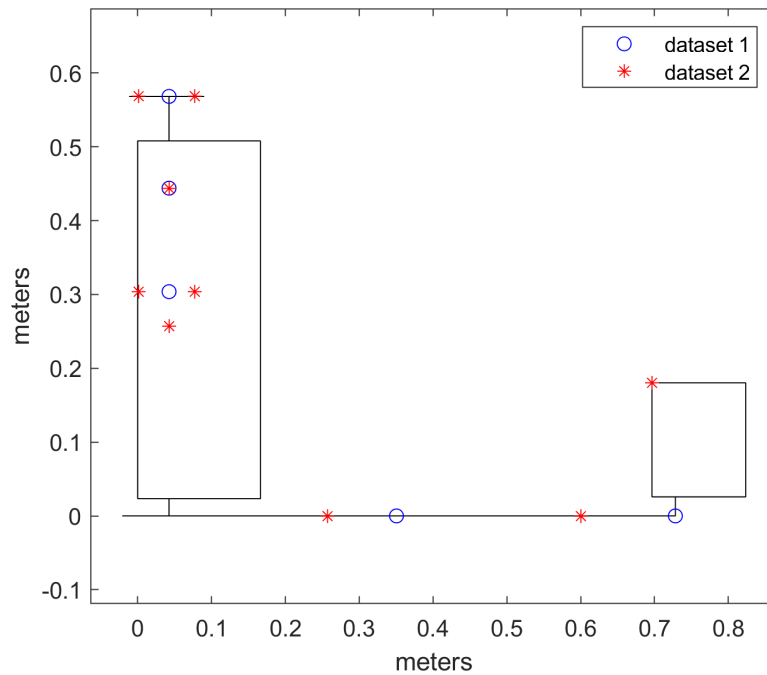


Figure 5.1: Accelerometer placement in ground vibration testing of MARGE

For the second dataset, pairs of accelerometers on the wing located a short distance apart chordwise were also treated as a fictional third accelerometer by taking the difference of their signals. This was done to simulate a sensor observing only torsional modes of the wing.

## 5.2 *Generating Frequency Response Functions*

Each GVT test point (input-output combination) was post-processed to generate the frequency response functions (FRFs) of the accelerometers to the impacts. This section describes the steps in this process.

### 5.2.1 *Time-Domain Post-Processing*

The time-series data was truncated to start just before the impulse input and end after  $t$  seconds where  $t$  was chosen to be at least four times the period of the lowest frequency of interest. (In most cases,  $t = 4$  seconds.) This ensured that irrelevant segments of the signal were eliminated while keeping still enough data to perform the frequency-domain analysis.

Each test point was recorded as three (in the second dataset) or five (in the first dataset) separate impacts. After truncation, the signals from these impacts were concatenated to form one continuous time-domain signal. The mean of this combined signal was then subtracted from it so that there would be no steady-state component before proceeding to compute the frequency response.

### 5.2.2 *Computing Frequency Response Functions*

The frequency response functions for each of these concatenated SISO signal pairs were computed using the method described in [?]. This section summarizes this method as it was implemented for the GVT data.

First, the signal was buffered into overlapping Hann windows and transformed using a chirp z-transform (CZT). The CZT is a generalization of the Discrete Fourier Transform (DFT) that can compute the Z-transform along an arc of the unit circle. Thus, it has an advantage over DFT in that it has the ability to allocate the full frequency-domain resolution to the bandwidth of interest. The purpose of first buffering the signal is to reduce the effect of noise at the expense of frequency resolution.

The products of the CZT are the power spectra of the signals. For any given accelerometer

power spectrum  $S_y$  and impact hammer power spectrum  $S_x$ , the frequency response function can then be computed as

$$FRF = \frac{G_{yy}}{G_{yx}} \quad (5.1)$$

where

$$G_{yx}(\omega) = S_y^* \cdot S_x \quad (5.2)$$

$$G_{yy}(\omega) = |S_y|^2 \quad (5.3)$$

The coherence can also be computed as

$$\text{coh}(\omega) = \frac{|G_{xy}|^2}{|G_{xx}||G_{yy}|} \quad (5.4)$$

where

$$G_{xy}(\omega) = S_x^* \cdot S_y \quad (5.5)$$

$$G_{yy}(\omega) = |S_y|^2 \quad (5.6)$$

The frequency response functions computed for the GVT data are shown in Appendix A.

### **5.3 Determining Modal Properties**

Once the FRFs were computed, the frequencies and damping ratios of the natural modes were determined from the FRFs.

#### *5.3.1 Computing Natural Frequencies*

First, visible natural frequencies visible as peaks in the data were noted. These often were visible across multiple FRFs, confirming that they were not artifacts from the noise of a single experimental trial.

These experimental natural frequencies were compared to those predicted by the NAS-TRAN finite-element model; if they matched well, it was assumed that the experimental

natural frequency corresponded to the mode shape generated by the NASTRAN model. This could be further validated by observing the antinodal points of the relevant NASTRAN mode shape and checking that the FRFs in which the natural frequency peaks are visible correspond to sensors placed near those antinodal points.

In some cases, there were clear natural modes visible in the experimental data that were not predicted by the NASTRAN finite-element model. It was inferred that two of these natural modes appeared in that these were torsional modes of the wing, because the FRFs they appeared most prominently in were from the aforementioned “fictional” accelerometers which had manipulated signals to enhance the response to torsional modes. These torsional modes were not predicted by the preliminary NASTRAN finite-element model; this was corrected in the subsequent FEM tuning process.

Each experimental natural frequency  $\omega_n$  was then measured in an automated way: first, all FRFs with a local maximum magnitude at  $\omega_n$  which was at least twice the magnitude of its surroundings was identified. The median of all of these measured natural frequencies, each from a different FRF, was then taken to be the true experimental natural frequency for that natural mode.

### 5.3.2 Computing Damping Ratios

The damping ratio was also measured in a similar automated way. The damping ratio was computed for each identifiable natural frequency in each FRF using the half-power method:

$$\zeta = \frac{\omega_2 - \omega_1}{2\omega_n} \quad (5.7)$$

where

$$\{\omega_1, \omega_2\} = \left\{ \omega \mid FRF(\omega) = \frac{1}{2} FRF(\omega_n) \right\} \quad (5.8)$$

The median of all of these damping ratios, each from a different FRF was then taken to be the true damping ratio for that natural mode. The experimentally obtained natural frequencies and damping ratios can be found in Table 5.1.

Table 5.1: Experimental Natural Modes

$\omega_n$	$\zeta$	Description
0		pitching
1.422	0.030	first wing bending
10.142	0.046	second wing bending
18.094	0.113	first wing torsion
19.893	0.033	first fuselate in-plane bending
19.897	0.031	first fuselage bending
32.545	0.019	third wing bending
51.706	0.084	second wing twisting
60.482	0.035	fourth wing bending
74.521	0.023	second fuselage bending

## Chapter 6

# **WIND TUNNEL VALIDATION AND MODEL TUNING**

The

## Chapter 7

### RESULTS

Lorem ipsum dolor sit amet, consectetur adipiscing elit. Sed sed erat vehicula elit sollicitudin ultrices at nec ligula. Sed non massa eget nibh pellentesque dapibus non at ante. Integer augue lacus, tincidunt vel sollicitudin fringilla, accumsan vitae lorem. Nunc eleifend scelerisque consectetur. Etiam justo nibh, hendrerit nec mattis non, tincidunt lacinia augue. Morbi ac enim hendrerit, iaculis ante eget, tincidunt massa. Morbi at justo sapien. Donec pulvinar urna id orci sodales, in ornare dolor venenatis. Quisque rutrum mi ac ornare tincidunt.

Sed semper luctus nisi eu tincidunt. Suspendisse gravida sapien libero, et facilisis velit facilisis a. Quisque lorem nisi, viverra a laoreet eu, semper nec nisl. Aliquam ligula lacus, finibus nec sapien et, iaculis pulvinar risus. Suspendisse vitae euismod ligula, vitae porta ipsum. Etiam tellus libero, suscipit id ultrices vitae, vulputate ut risus. Proin ultricies elementum nisi, cursus eleifend velit lacinia nec. Praesent eu quam eu nulla imperdiet varius a ac urna. Suspendisse tristique purus in massa sagittis, vel varius nibh mattis. Donec eget est malesuada, mollis nisl id, dapibus lacus. Aenean aliquam quam in nisl volutpat ultrices.

Sed porta ligula et porttitor lacinia. Aliquam quis nisi vel orci hendrerit lacinia at at risus. Sed condimentum, lectus at elementum facilisis, ante ipsum placerat nibh, eu accumsan metus libero gravida arcu. Aenean et tempus magna, aliquam semper magna. Nulla facilisi. Quisque efficitur dui non lobortis rutrum. Nullam vulputate nec nulla ut suscipit. Nunc et iaculis lacus. Duis aliquam pretium justo, eget finibus sem auctor non. Nulla venenatis ac leo a sodales. In ut rhoncus nibh. Aenean at viverra arcu. Proin accumsan nisl sit amet consectetur pharetra.

## Chapter 8

### CONCLUSION

Lorem ipsum dolor sit amet, consectetur adipiscing elit. Sed sed erat vehicula elit sollicitudin ultrices at nec ligula. Sed non massa eget nibh pellentesque dapibus non at ante. Integer augue lacus, tincidunt vel sollicitudin fringilla, accumsan vitae lorem. Nunc eleifend scelerisque consectetur. Etiam justo nibh, hendrerit nec mattis non, tincidunt lacinia augue. Morbi ac enim hendrerit, iaculis ante eget, tincidunt massa. Morbi at justo sapien. Donec pulvinar urna id orci sodales, in ornare dolor venenatis. Quisque rutrum mi ac ornare tincidunt.

Sed semper luctus nisi eu tincidunt. Suspendisse gravida sapien libero, et facilisis velit facilisis a. Quisque lorem nisi, viverra a laoreet eu, semper nec nisl. Aliquam ligula lacus, finibus nec sapien et, iaculis pulvinar risus. Suspendisse vitae euismod ligula, vitae porta ipsum. Etiam tellus libero, suscipit id ultrices vitae, vulputate ut risus. Proin ultricies elementum nisi, cursus eleifend velit lacinia nec. Praesent eu quam eu nulla imperdiet varius a ac urna. Suspendisse tristique purus in massa sagittis, vel varius nibh mattis. Donec eget est malesuada, mollis nisl id, dapibus lacus. Aenean aliquam quam in nisl volutpat ultrices.

Sed porta ligula et porttitor lacinia. Aliquam quis nisi vel orci hendrerit lacinia at at risus. Sed condimentum, lectus at elementum facilisis, ante ipsum placerat nibh, eu accumsan metus libero gravida arcu. Aenean et tempus magna, aliquam semper magna. Nulla facilisi. Quisque efficitur dui non lobortis rutrum. Nullam vulputate nec nulla ut suscipit. Nunc et iaculis lacus. Duis aliquam pretium justo, eget finibus sem auctor non. Nulla venenatis ac leo a sodales. In ut rhoncus nibh. Aenean at viverra arcu. Proin accumsan nisl sit amet consectetur pharetra.



Appendix A

**FREQUENCY RESPONSE FUNCTIONS**

